UNIVERSITY OF AMSTERDAM

UvA-DARE (Digital Academic Repository)

Angle-resolved cathodoluminescence nanoscopy

Coenen, T.

Publication date
2014

Link to publication

Citation for published version (APA):
Coenen, T. (2014). *Angle-resolved cathodoluminescence nanoscopy*. [Thesis, externally prepared, Universiteit van Amsterdam].

General rights
It is not permitted to download or to forward/distribute the text or part of it without the consent of the author(s) and/or copyright holder(s), other than for strictly personal, individual use, unless the work is under an open content license (like Creative Commons).

Disclaimer/Complaints regulations
If you believe that digital publication of certain material infringes any of your rights or (privacy) interests, please let the Library know, stating your reasons. In case of a legitimate complaint, the Library will make the material inaccessible and/or remove it from the website. Please Ask the Library: https://uba.uva.nl/en/contact, or a letter to: Library of the University of Amsterdam, Secretariat, P.O. Box 19185, 1000 GD Amsterdam, The Netherlands. You will be contacted as soon as possible.

UvA-DARE is a service provided by the library of the University of Amsterdam (https://dare.uva.nl)

Download date:04 Nov 2026

9

Optical properties of individual plasmonic holes probed with local electron beam excitation

Just like nanoparticles, nanoscale holes form a basic building block in nanophotonic devices. In this Chapter we study the spectral and angular cathodoluminescence response of individual nanoholes with diameters ranging from 50 to 180 nm. We find that the holes can be excited efficiently at the edge of the hole and that the response becomes stronger in the near-infrared part of the spectrum for larger holes. Using finite-difference time-domain simulations we characterize the resonant modes inside the holes. By using ARCIS we are able to measure the angular response and observe strong beaming towards the side of electron beam excitation, complementary to what was shown for nanoparticles. We find that the angular response can be explained by assuming a coherent superposition of radiating dipole moments, where the contribution of in-plane magnetic and electric dipole components increases for larger diameters.

9.1 Introduction

Nanoscale apertures form a basic building block for plasmonic devices [211]. Similar to nanoparticles, such nanoscale holes and slits have the ability to strongly

confine light due to localized plasmon resonances that are supported by the structure, which for example allows strong enhancement of fluorescence [212]. On the other hand, since a hole is the geometrical inverse of a nanoparticle its transmission and reflection properties are complementary to that of a particle (Babinet's principle) [33, 74, 211, 213–215], although strictly speaking this only holds for 2D structures in a perfectly conducting film [216]. Furthermore, subwavelength holes diffract light in quasi-cylindrical waves (QCWs) and can couple to bound surface plasmon polaritons (SPPs) in plasmonic films which provide extra channels through which holes can be excited and coupled [217–221]. These coupling mechanisms have been utilized in ordered arrays to obtain extraordinary transmission [211, 222] and absorption [223], where the transmission/absorption cross section exceeds the geometrical cross section of the holes. Due to their accessible open geometry and unique transmission and absorption characteristics, plasmonic holes may find applications in CMOS cameras as color filters [52, 53] and nanoscale sensors [42, 47, 48].

Although the collective optical properties of holes in arrays have been studied extensively, characterization of individual holes is difficult owing to their subwavelength size. It has been demonstrated that by using scanning near-field microscopy the fundamental scattering properties can be measured [220, 224]. Alternatively, experimental techniques that employ a fast electron beam as excitation source, like electron energy-loss spectroscopy (EELS) and cathodoluminescence (CL) spectroscopy, have been used to reveal the resonant properties of circular holes [225], rectangular holes [226], nanoslits [74, 215], and inverse split rings [227]. In this Chapter we aim to further elucidate the local optical response of individual deep-subwavelength plasmonic holes, by using Angle-Resolved CL Imaging Spectroscopy (ARCIS).

9.2 Sample fabrication

We deposited a 80 nm thick gold layer on a silicon substrate using thermal evaporation. To reduce the granularity of the film we evaporated a 1 nm thick seed layer of germanium first [228, 229]. Subsequently we used focused-ion-beam (FIB) milling to pattern circular holes in the film, with diameters D ranging from 50 – 180 nm in steps of 5 nm and a depth of 80 nm (we stop the milling process at the silicon interface). To obtain the best patterning resolution we used a low ion-beam current (1.5 pA). Electron micrographs of the resulting structures are shown as insets in Fig. 9.1(a). Inherent to the FIB milling process there is some tapering of the hole due to material redeposition. The lowest-order propagating mode in a circular hole is cut off for wavelengths larger than the cutoff wavelength (λ_{cutoff}). $\lambda_{cutoff} \approx 1.7D$ [211], which for D = 180 nm holes, corresponds to λ_0 306 nm. Therefore we expect that the fundamental waveguide mode is cut off in the visible/near-infrared (NIR) regime for the holes that are considered in this experiment. The transmission through a 80 nm thick gold film is < 5% for this wavelength range as calculated by an

analytical Fresnel code, so any direct transmission through the gold film is strongly attenuated.

9.3 Spectral response measurements

We first measure the local spectral response of the holes (see Chapter 2 for details on experimental setup). To that end we raster scan the electron beam (30 keV acceleration voltage, 0.8 nA current) in 5 nm steps for $D \leq 100$ nm and 10 nm steps for $D > 100$ nm, using an integration time of 1 s per pixel. Figure 9.1(a) shows the spatially averaged spectrum for D = 50 nm, D = 100 nm, and D = 180 nm holes respectively. The spectra are corrected by subtracting the transition radiation (TR) from an unstructured part of the gold film and multiplying with the system response. The system response was calibrated using the same TR radiation. Because

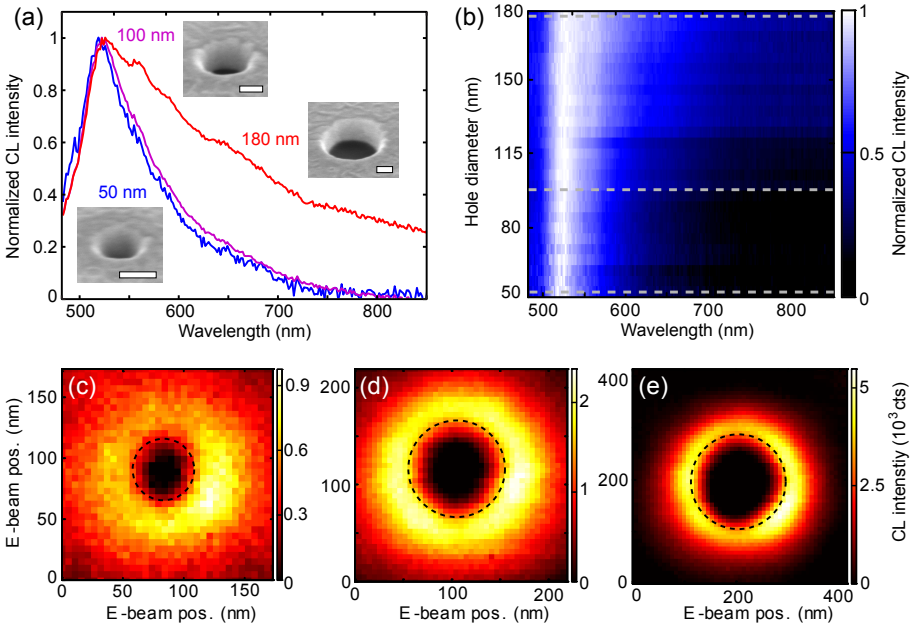


Figure 9.1: (a) Spatially-integrated normalized CL spectra for Au nanoholes with D = 50, 100, and 180 nm. Scanning electron micrographs of the corresponding holes are shown as insets in which the scale bars represent 50 nm. The images were taken at a 52° sample tilt. (b) Integrated peak-normalized CL spectra for a range of different nanohole diameters in 5 nm steps. The gray dashed lines indicate diameters for which spectra are shown in (a). CL intensity as function of excitation position for (c) D = 50 nm(d) D = 100 nm, and (e) D = 180 nm at λ_0 = 520 nm, integrated over a 20 nm bandwidth. The black dashed circles indicate the edge of the hole.

the signal within the hole is lower than the TR background we get negative intensity values inside the hole, so we mask this area to obtain the integrated spectrum such that it does not artificially perturb the spectrum. For D = 50 nm and D = 100 nm holes we observe a relatively narrow peak centered around λ_0 = 520 nm. For D = 180 nm the peak wavelength is still around 520 nm but now the peak now is much broader with a long tail extending into the NIR regime. Because this hole is significantly larger in size, a stronger response in the red/NIR part of the spectrum can be expected. Fig. 9.1(b) shows the spatially integrated spectrum for all studied hole diameters in which we can clearly see the gradual broadening of the response for larger diameters.

It is also insightful to study the spatial excitation profiles of the holes. Figures 9.1(c-e) show the spatial distributions at λ_0 = 520 nm. For all diameters we observe a bright ring around the hole, whereas the hole itself remains dark. For excitation in the center of the hole the evanescent electron fields cannot polarize the metal because the edges are too far away so efficient driving of a p_z component in the center is not possible like is the case for the nanoparticles (see Figs. 8.1 and 8.4). Furthermore, any radiation that is generated at the silicon interface or in the silicon bulk cannot efficiently couple to free-space radiation into the upper angular hemisphere because the waveguide mode in the hole is beyond cutoff for these diameters. Similar spatial excitation profiles were observed in Ref. [225], although those were measured on a free-standing silver film. We note that the larger holes are significantly brighter than the smaller holes. This is quantified in Fig. 9.2(a) where we compare the maximum signal strength at the hole $I_{tot}(\lambda_0)$ with the constant TR background $I_{TR}(\lambda_0)$ by plotting $(I_{tot} - I_{TR})/I_{TR}$ for different diameters and wavelengths. Such a trend is expected as larger holes should scatter more efficiently into the far field.

9.4 CL signal decay away from the hole

To better understand the excitation processes that are involved in the CL experiment we study the decay of the CL signal away from the hole. This is visualized in Fig. 9.2(b) where we plot the CL-intensity (with the TR-background subtracted) as function of the radial distance from the hole center at λ_0 = 520 nm, extracted from the images shown in Fig. 9.1(c-e). The signal decays rapidly away from the hole edge. The $1/e$ distance corresponds to ~35 nm for each hole diameter. Within this spatial region we expect that there is direct coupling to the near-field of the hole resonance. Because of the surrounding gold film, indirect excitation of the holes is also possible through SPPs that are generated by the electron beam away from the hole and subsequently scattered out by the hole.

The interaction with such a circular SPP wave would rapidly decay as function of distance to the hole. We estimate this decay length with a simple intuitive model. First of all, the degree of interaction of the hole with the SPP wave drops as the electron beam moves away further from the hole due to the decreasing 2D acceptance

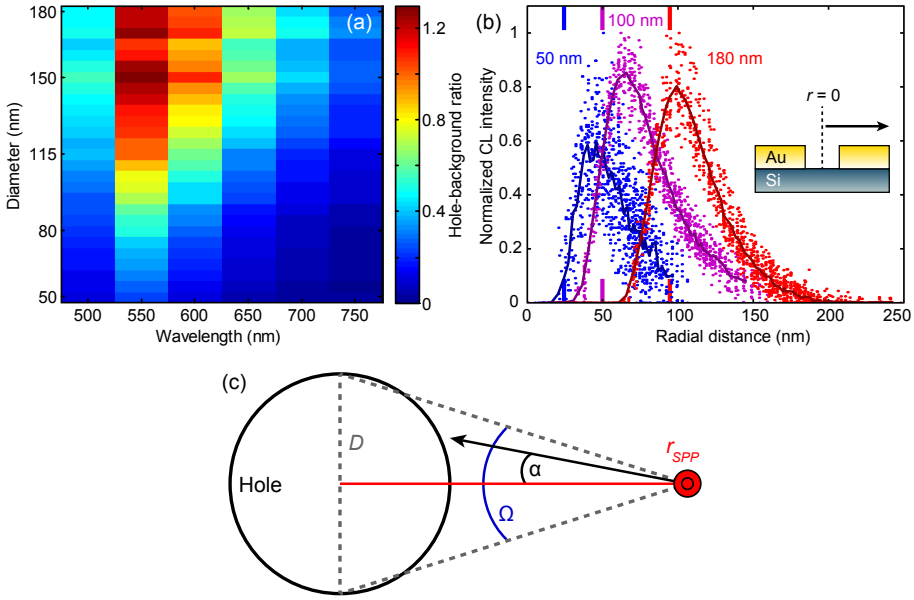


Figure 9.2: (a) Hole-signal to TR background ratio where the color-map represents $(I_{tot} - I_{TR})/(I_{TR})$. To compare to the angular measurements and for better signal-to-noise ratio we use 50 nm wavelength bins. (b) Radial dependence of CL signal from the hole at λ_0 = 520 nm (averaged over a bandwidth of 20 nm) for D = 50 nm (blue), D = 100 nm (magenta), and D = 180 nm (red). Each dot represents a CL pixel to which we assign a radial distance from the hole center. The solid curves represent the average value of 20 binned datapoints. (c) Schematic representation of the interaction of a circular SPP wave with a hole. The geometrical parameters used in the model are indicated in the figure.

angle ($\Omega = \tan^{-1}(\frac{D}{2r_{SPP}})/\pi$) covered by the hole. This effect can be gives rise to a rapid decrease in signal for increasing r_{SPP}, where r_{SPP} is the position at which the SPP wave is generated (at the beam impact position) relative to the hole center. This is schematically indicated in Fig. 9.2(c). For this calculation we neglect any effects of hole shape and effective scattering cross sections that are either larger or smaller than the hole diameter.

Second, the SPPs also experience Ohmic loss, while propagating towards the hole. In order to quantify the propagation losses we need to know the dispersion characteristics of the SPPs. Using an analytical mode solver we have calculated the dispersion relation for the guided SPP modes in our layered system. We find that the layer supports two plasmon modes, which exhibit very similar dispersion to the single-interface plasmon modes for a vacuum-gold and silicon-gold interface respectively, indicating that there is little coupling between the top and bottom interface of the gold film. The guided plasmon mode on the silicon-gold interface is heavily damped and will couple poorly to free space radiation in the upper angular

hemisphere as it has to couple out through the hole. Hence we expect that the CL response is dominated by SPPs from the top interface. As the propagation length L_{SPP} for this mode is generally larger than 350 nm (calculated from Im$\{k_{SPP}\}$ using the analytical mode solver calculations), the effect on the overall signal decay is relatively small compared to the acceptance angle losses.

There is some dependence in the SPP propagation decay on the angle α with respect to the axis that is defined by the electron beam position and the hole center (see Fig. 9.2(c)), which leads to a $\exp(\frac{-r_{SPP}}{L_{SPP}\cos(\alpha)})$ term for the propagation loss [230]. For small acceptance angles $\alpha \simeq 0$ and the SPP decay reduces to $\exp(\frac{-r_{SPP}}{L_{SPP}})$. For structures that have a more significant transverse spatial extend ($D \gg r_{SPP}$) like gratings the acceptance angle remains constant at a value close to π for any r_{SPP}. Hence, the angle-dependent SPP propagation losses are the dominant decay mechanism in that case which can be used to study plasmon propagation lengths on metal films [64, 230, 231].

Taking into account the decrease in acceptance angle and the Ohmic losses, we find 51, 90, and 140 nm decay lengths from the hole edge (for λ_0 = 520 nm) for D = 50, 100, and 180 nm, respectively. However, in the experiment there is no noticeable diameter dependence in the CL signal decay. Also, the decay occurs over significantly shorter distances suggesting that the direct near-field coupling dominates the CL-experiment.

9.5 Simulation results

To gain more insight into the resonant properties of these holes we perform finite-difference time-domain simulations (FDTD) [232]. In particular, we use a total-field scattered-field source to calculate the scattering spectra for hole diameters between 50 and 180 nm (in 10 nm steps) under plane-wave illumination at normal incidence (the simulation setup is similar to what is described in Fig. 10.9). We use tabulated optical constants for silicon [139] and gold [114]. Figure 9.3(a) shows the normalized upward scattered power spectrum for the same diameters as in Fig. 9.1(a). Similar to the experiment we only consider the upward scattered power. The effective NA of the top monitor is 0.85. We note that the total scattered power spectrum (not shown here) looks very similar to the upward scattered power indicating that upward scattered power is representative for the overall scattering response in this case. In order to calculate the total scattered power the silicon substrate was approximated by a n = 4 lossless dielectric such that the light that is scattered down into the substrate is not attenuated by absorption in the silicon before it reaches the power monitor.

Figure 9.3(b) shows the evolution of the spectrum in the range D = 50 – 180 nm (calculated in 10 nm steps). The scattering spectrum only changes moderately with diameter, similar to what is observed in the CL experiment. We note that the normalized scattering cross sections Q_{scat} (normalized to the hole area) are quite low (Q_{scat} = 1.1 for D = 180 nm at the peak wavelength of 575 nm) compared

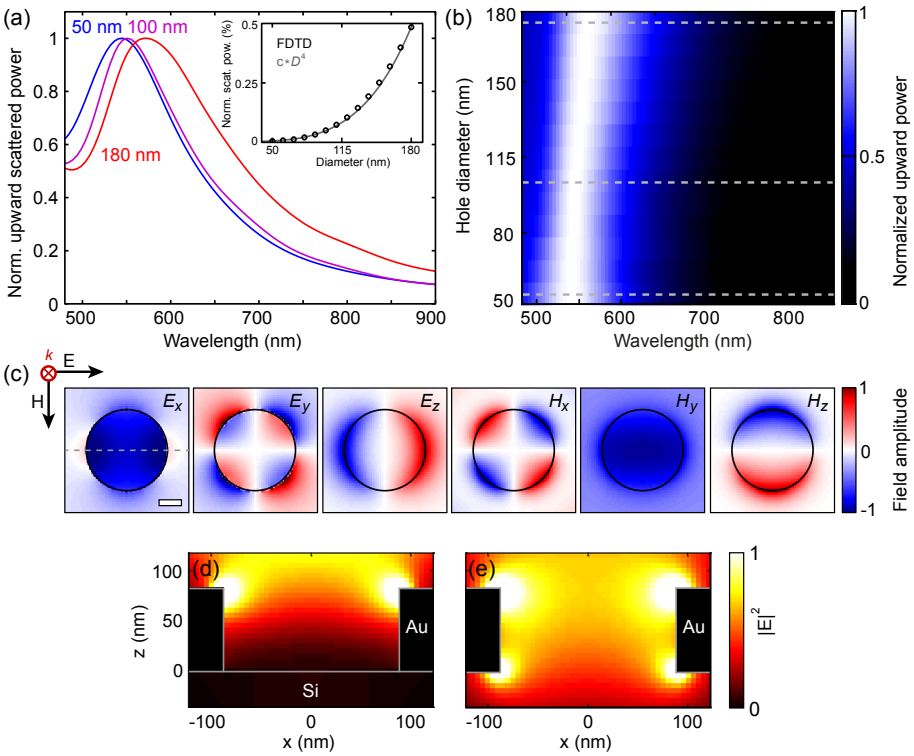


Figure 9.3: (a) Upward scattering for $D = 50$, 100 and 180 nm holes for plane-wave excitation under normal incidence, calculated using a TFSF simulation in FDTD. We only plot the part of the light that is emitted upwards as that is the part that is collected in our CL system. The spectra have been normalized to 1 for visibility as the largest hole scatters much more strongly than the smallest one. The inset in shows the amount of upward scattered power relative to the incoming power as function of diameter (black circles), integrated over the full spectral range. Through the data we have fitted a D^4 curve (gray curve) that has been scaled by a constant ($c = 4.7 \times 10^{-10}$). (c) In-plane field (xy) cuts for $D = 180$ nm at $\lambda_0 = 575$ nm showing the real part of E_x, E_y, E_z, H_x, H_y, and H_z respectively. The cuts are taken at half height, 40 nm above the substrate. For reference we have included the incoming plane-wave polarization. The scale bar is 50 nm. Out-of-plane (xz) cuts showing the near field intensity ($|E|^2$) for the same hole with (d) and without (e) silicon substrate at $\lambda_0 = 570$ and 620 nm, respectively. The position of the cut in the xy-plane is indicated by the gray dashed line in the E_x map in (c).

to those for nanoparticles. This could be related to the fact that a hole has less polarizable metal available for a given geometrical cross section. In the inset of Fig. 9.3(a) we show the amount of upward scattered power integrated over the full spectrum for different hole diameters, normalized to the incident power in the simulation. We observe a superlinear increase in the amount of scattered power

for larger holes which is proportional to D^4 in this size range. This is consistent with the notion that the emitted power for dipoles is proportional to the square of polarizability which itself generally scales with volume. In this case the effective hole volume increases by D^2 for increasing diameter leading to a D^4 overall power dependence.

By studying the induced near-field distributions one can identify the nature of the resonant peak. Figure 9.3 shows all six electric and magnetic field components for an in-plane cut at half-height (40 nm above the silicon substrate for D = 180 nm at λ_0 = 575 nm). The electric and magnetic fields show a mix of in-plane electric and magnetic dipole contributions. The fields are consistent with a p_x electric dipole moment and m_y magnetic dipole moment, commensurate with the incoming plane-wave electric and magnetic field polarizations. Furthermore, it is clear that there is a significant E_z contribution near the edge of the hole, which is the electromagnetic field component to which the electron beam couples efficiently. The dipole modes we observe here are infinitely degenerate due to the circular symmetry of the hole, which is why we observe a bright ring in the excitation maps in Fig. 9.1(c-e), rather than the E_z profile calculated with FDTD which shows two hotspots along the polarization direction. The $1/e$ decay value for $|E_z|^2$ is ~20 nm away from the hole edge where the field is maximum, which is slightly shorter than the experimental values obtained with CL (see Fig. 9.2(b)). Possibly, this is related to the fact that in the FDTD we have a perfectly cylindrical hole, whereas in the experiment the edge is rounded which could smear out the intensity profile. The field maps were also calculated for the other diameters and free-space wavelengths and show similar patterns to Fig. 9.3(c).

Interestingly, we find that when we remove the silicon substrate in the simulations, the holes scatter more strongly (Q_{scat} = 3 at the peak wavelength of 630 nm) and also experience a stronger redshift for larger diameters. In the near-fields we still clearly observe the in-plane magnetic and electric dipole fields. It is well-known that a substrate can strongly influence the scattering of dipolar scatterers through the Drexhage-like change in the local density of optical states that it imposes on the position of the scatterer [210, 233, 234]. For a perfectly conducting mirror, the radiative emission from an in-plane electric dipole is suppressed whereas for an in-plane magnetic dipole it is enhanced when close to the mirror. For silicon the situation is different and the emission from both electric and magnetic dipoles is enhanced [234] which is the opposite of what we find in our simulations where the silicon substrate leads to a reduction in the scattering. One possible reason could be that an emitter-mirror configuration does not adequately describe the scattering of a hole due to the surrounding gold layer which potentially could exhibit additional mirror charge effects.

While mirror-like interference effects could have an influence on the hole scattering, the plane-wave driving efficiency of the hole also plays a significant role. When a wave reflects off the silicon substrate, the electric field approximately undergoes a phase shift of approximately π, leading to destructive interference close to the interface [235]. This is corroborated by the near-field distributions for the

cases with and without substrate, which are shown in Fig. 9.3(d,e). This driving interference effect is more pronounced for longer wavelengths as the destructive interference extends over a longer range away from the surface which explains the blue-shifted response of the hole. However, in order to suppress the driving efficiency there must be significant intensity in the reflected wave and this is not the case for small D/λ_0 ratios as the incoming wave is too strongly attenuated. The latter effect dominates for D = 50 nm, where the scattering cross sections with and without substrate are similar, whereas for D = 180 nm the driving interference does play a significant role.

9.6 Angular response

For sensing applications, the angular emission profile of the hole when coupled to a local emitter can be of significant importance. In this Section we study the angular response of the holes when excited by an electron beam. It has been shown that holes/slits surrounded by grating-like corrugations can be highly directional emitters of free space light [174] or SPPs [236] which can be used to enhance and direct fluorescence originating from the hole for instance [173, 237]. Even unstructured holes/slits can act as directional emitters owing to the fact that they support electrical dipole as well as magnetic dipole modes that can interfere in the far field (Kerker effect) [189, 224, 238]. To study the directionality of holes we measure the angular emission pattern using ARCIS. We collect angular patterns while exciting a single hole at four orthogonal edge positions (left, right, top, and bottom) for center wavelengths λ_0 = 400 – 750 nm in 50 nm steps using band pass filters (40 nm bandwidth). We do not collect an angular pattern for excitation at the center of the hole as there is practically no CL emission at that position. For the angular patterns we cannot subtract the background radiation pattern from a bare gold substrate which corresponds to a symmetric torus (see Fig. 3.3), as that leads to negative emission values for certain angles.

Figure 9.4 shows angular patterns for a D = 100 nm hole measured for top (1), right (2), bottom (3), and left (4) edge excitation as indicated by the schematics below the angular patterns. Similar to the nanoparticles in Chapter 8, the angular pattern co-rotates with the excitation position which means that a different combination of multipole components is excited at each position. Light is scattered towards the direction of the excitation point thus opposite to what was observed for the nanoparticles (see Fig. 8.2), illustrating the complementarity between the two geometries. The backward-to-forward scattering ratio calculated by dividing the integrated backward half of the angular hemisphere by the forward half, is quantified in Fig. 9.5(a) for different diameters and wavelengths. Here backward is defined as towards the excitation position and forward is defined as away from the excitation position. For all measurements we observe dominant backward scattering (ratio being larger than 1) although for smaller diameters the directionality moves more quickly towards 1 for increasing wavelength. This is to be expected as the

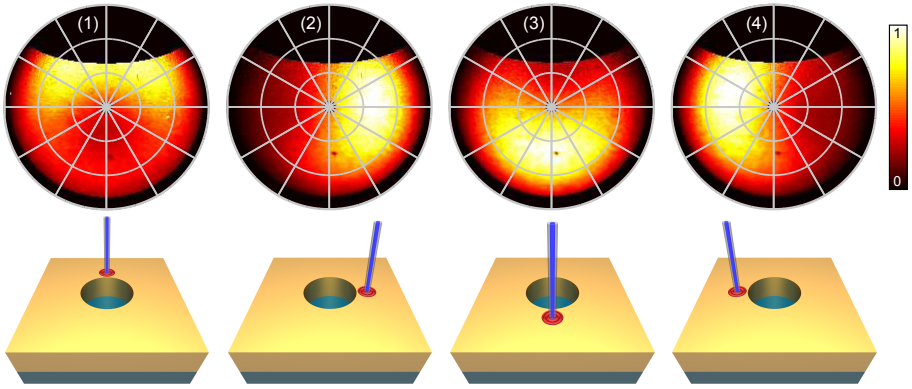


Figure 9.4: Experimental normalized angular cathodoluminescence emission patterns collected from a 100 nm diameter nanohole at λ_0 = 500 nm for excitation near the edge for four orthogonal azimuthal angles (same coordinate system as in Fig. 8.2): (1) 0° (top), (2) 90° (right), (3) 180° (bottom), and (4) 270° (left). The excitation positions are indicated by the schematics below the patterns. The patterns have been normalized to the maximum intensity value for all four patterns to show the relative brightness for different excitation positions.

smallest holes do not scatter efficiently in the red leaving the azimuthally symmetric TR emission as the dominant source of radiation (see also Fig. 9.2(a) for the ratio between hole scattering and TR signal).

Contrary to what was found for the nanoparticles, varying the diameter does not have a very profound influence on the directionality. This is emphasized in Figs. 9.5(b) where we show angular patterns for D = 50, 100, 140, and 180 nm at λ_0 = 500 nm for excitation on the left edge of the hole. The patterns look very similar. Figure 9.5(c) shows cross cuts through the patterns in (b), integrated over a range of ϕ to improve the signal-to-noise ratio. For increasing diameter we observe a slow but gradual shift in the pattern towards the normal suggesting that the in-plane components become more dominant.

Based on the FDTD simulations, we know that the hole supports in-plane electric and magnetic dipole modes. From the driving symmetry we expect that for excitation on the left side of the hole we can excite a p_x and m_y component. When we move towards the top of the hole the excited moments would co-rotate and we would have a p_y and m_x component, related to the circular degeneracy of the resonant modes. Although interference between these in-plane dipole components can lead to enhanced out-of-plane upward-or downward scattering [191, 192, 195, 235] it cannot explain the backward-forward asymmetry in our angular measurements. Such an asymmetry requires an out-of-plane dipole component as well. In our experiment we generate TR emission at the edge of the hole which has an effective p_z dipole moment. As is clear from Fig. 9.2(a) the TR contribution is significant and can interfere with the radiation scattered by the hole, similar to

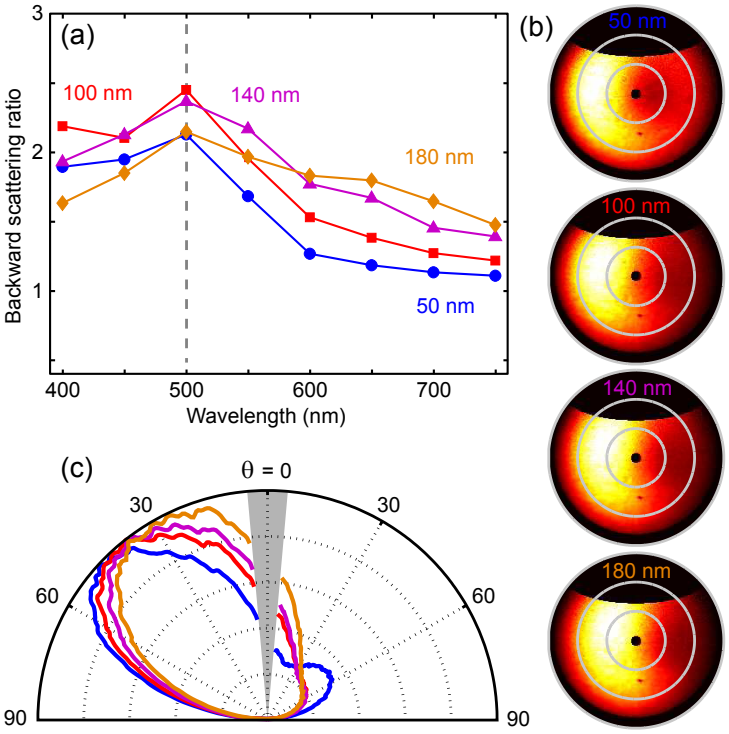


Figure 9.5: (a) Backward-to-forward scattering ratio as function wavelength for different hole diameters. The data was averaged over two excitation positions (left and right) (b) Angular patterns for D = 50, 100, 140, and 180 nm at λ_0 = 500 nm, as indicated by the gray dashed line in (a). (c) Cross cuts through radiation patterns in (b), plotted with the same color code as in (a). The crosscuts have been integrated over a range of ϕ ($\phi = 60 - 120^\circ$ and $\phi = 240 - 300^\circ$) as indicated in Fig. 8.2(a) by the blue dashed lines. All patterns in (c) have been normalized to 1. No data is collected for the gray region which corresponds to the angular range that is taken by the hole in the parabolic mirror.

what was observed for gratings [112]. Furthermore the hole itself can also support a p_z component [216, 220] which could be driven by the electron beam. These two potential p_z contributions are difficult to separate in this experiment.

Regardless of the origin of the p_z component, we expect that the resulting angular pattern is caused by coherent interference of p_z, p_x, and m_y dipole moments. As a simple estimate for the angular patterns we can take the coherent sum of a p_z moment and in-plane components m_y and p_x where we use the ratios from Fig. 9.2(a) as the ratio between the out-of-plane and in-plane components. To take into account substrate interference we assume that the dipoles are located at a vacuum-gold interface. In our model we place the m_y and p_x components

corresponding to the hole resonance at the center of the hole, whereas the p_z component is positioned at the edge of the hole representing the TR emission at the electron beam impact position (spaced by a distance $D/2$ from the hole center). Finally, we assume a fixed phase relation between all the components and equal m_y, and p_x contributions.

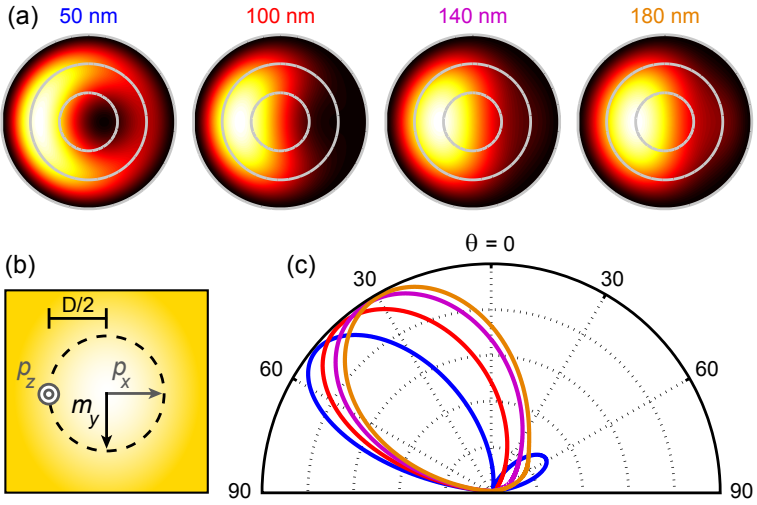


Figure 9.6: (a) Angular patterns for a combination of p_z, p_x, and m_y, where the ratios between in-plane and out-of-plane components for the different hole diameters are taken from Fig. 9.2(a). This combination of dipole moments is expected for excitation on the left edge of the hole. (b) Schematic top view of the dipole orientations with respect to the hole (included as circular dashed line for reference) as used in the model. We position the p_z dipole at the edge of the hole at the electron impact position. (c) Cross cuts through (a) using the same color code and integrated over the same range of ϕ as in Fig 9.5(c).

Figure 9.6(a) shows the calculated angular radiation patterns for the coherent interference between dipole moments taking the assumptions mentioned above. A top view of the dipole configuration is shown schematically in (b). In (c) we show the cross cuts through the patterns in (a) similar to Fig. 9.5(c). Although this model is very simple and is based on several assumptions it already gives remarkably good agreement with the experimental data. Because the in-plane components become stronger for larger diameters, the emission lobe moves towards the normal for larger holes, going from $\theta = 50°$ to $\theta = 30°$, which matches well with the data in Fig. 9.5(c). Furthermore, for the smallest diameter the p_z component is relatively strong which leads to a small forward lobe. This additional lobe is also visible in the CL data (see Fig. 9.5). We note that angular emission profiles of the nanoparticles had significant quadrupolar contributions but for the holes these do not seem to be necessary to explain the data. The fact that the hole response

appears to be mainly dipolar agrees well with our plane-wave simulation results and with results obtained by Rotenberg *et al.* [220, 224], even though the local electron beam driving creates stronger gradients that potentially could enhance higher order moments [207]. The far-field directionality in this experiment is complementary to the directionality that was observed in the near field [224], although in that case the holes were driven through SPPs which cannot efficiently drive an electric dipole moment along the propagation direction due to its transverse-magnetic wave nature. Furthermore there was no TR emission component present in those experiments, as that is unique to electron-beam excitation.

9.7 Conclusions

In conclusion, we have used angle-resolved cathodoluminescence spectroscopy to unravel the local response of individual nanoscale holes patterned in a gold film. We studied the influence of hole diameter on the scattering spectrum and angular radiation profile. In the spectra we find a strong contribution around λ_0 = 520 nm for all diameters. The response in the red/NIR spectral region increases for larger diameters. By studying the decay of the CL signal away from the hole, we determine that direct coupling to the hole resonance near-fields is the main source of coupling. Using finite-difference time-domain simulations we further elucidate the scattering behavior. We find that the scattering of the holes is suppressed due to the substrate. Furthermore, we deduce from the induced near fields that the emission has both electric and magnetic dipole character. The interference of these in-plane components with an out-of-plane electric dipole moment gives rise to transverse beaming by the holes, complementary to what was found for nanoparticles before. As the diameter increases the in-plane dipole components become more dominant, leading to a shift in the main emission lobe towards the normal. This behavior is well-reproduced by a simple dipole-interference model where we take the spectral measurements as input to determine the ratio between the in-plane and out-of-plane components. These insights could be used in the future to design and characterize novel plasmonic devices based on holes for color filtering and sensing applications.